LES-based simulation of the time-resolved flow for rotor-stator interactions in axial fan stages

Jesús Manuel Fernández Oro*, Andrés Meana-Fernández, Mónica Galdo Vega, Bruno Pereiras García, José González Pérez

Fluid Mechanics Area, Department of Energy, University of Oviedo
C/Wifredo Ricart s/n Gijón Asturias 33203 Spain

Abstract

Mechanisms related to rotor-stator interaction in an axial flow fan at a typical Reynolds number of $8.5 \cdot 10^5$ (based on the blade chord) have been investigated using a Wall-Modeled Large Eddy Simulation (WMLES). Computations were performed for three different operating conditions, from nominal (Q_N) to off-design (85 and 70 Q_N) working points, for a spanwise 3D extrusion of the central section of the fan stage. Circumferential periodic conditions (comprising 40 deg.) were introduced to simulate a reduced 2 blades/3 vanes domain with respect to the original full-annulus geometry. Also, useful guidelines for statistical convergence of the LES computations in multistage fan environments are provided and contrasted. The objective of the numerical simulations is the analysis of the rotor wakes transport and both wake-vane and wake-wake interactions in the stator flow field. Special attention is devoted to off-design conditions where the description of massive flow separations in the vane suction side takes full advantage of the LES performance. Rotor wakes (their associated vortical structures) impinging on the vanes set off a coherent shedding of large-scale vortices at reduced frequencies (between 0.1 to 0.25 of the Blade Passing Frequency BPF) while the pressure coefficient in the vanes remains practically unaffected by this effect in the separated region. On the contrary, on the LE of the vane, the interaction is manifested as large fluctuations of the pressure coefficient in the stagnation region. These numerical evidences have been experimentally confirmed using previous hot-wire measurements in the outer-half of the fan span where radial velocity components of the flow are negligible. Turbulent scales and wake profiles, both meantime and time-resolved, validate the numerical framework adopted. In addition, the detailed analysis of the off-design conditions demonstrates the accurate description of coherent vortical structures and length scales with the LES computations.

Keywords: axial fan stage; rotor-stator interaction; time-resolved flow; LES modeling; integral scales; turbulence

*Corresponding author: jesusfo@uniovi.es

1. Introduction

Nowadays, CFD techniques have achieved a notable level of maturity, so its regular use for the analysis and prediction of turbomachinery performance is already a standard in the industry [1]. Unfortunately, major concern is still placed on the accurate assessment of the turbulent characteristics of the flow [2], especially in the case of multistage environments at off-design conditions. URANS simulations with complex turbulence models, mainly for industrial applications, can provide good results for design conditions, but as the flow gains in complexity, these tools can underpredict or even neglect significant flow features. Moreover, in multi-row configurations, strong interaction phenomena and complex vortical structures may arise due to moving surfaces. Hence, unsteady flow and turbulence generation (vortex shedding, wake-wake interaction, wake chopping and diffusion) may require a more detailed treatment of the turbulent scales.

Despite the high Reynolds numbers, Large Eddy Simulations (LES) are becoming a feasible option for the numerical analysis of the flow within turbomachinery, where the turbulent flow has a wide span of scales, ranging from large eddies in the order of the primary flow to the Kolmogorov scales for small turbulent dissipation [3]. In LES computations, all the turbulent vortices of the same order of magnitude as the mesh density are explicitly resolved, while the lower scales subgrid scales- are modeled [4]. This is a great advantage because macroscopic scales are difficult to model due to its anisotropic nature and its large dependence on the characteristics of the geometry and the main flow [5]. However, the price to be paid is that high-resolution meshes and large CPU times are required to obtain a full statistical convergence of the results. Furthermore, a full-LES modeling is still not realistic for industrial applications in turbomachinery at present day because wall-resolving models demand the same strict resolution requirement of DNS in the inner region of the boundary layer [6]. Hence, the only practical way to perform reliable LES of high-Re numbers ($10^5 < \mathrm{Re} < 10^7$) is by computing the outer layer only. The use of wall-modeling (or hybrid LES/RANS techniques), in combination with blade/vane rescaling, is employed to make the LES computational costs practicable in multistage turbomachinery [7]. Recent reviews [8] confirm that practical LES simulations are becoming a real option after the validation of key issues like the influence of BCs, wall-modeling, mesh topology or sub-grid scale modeling is properly assessed [9].

Complementary, post-processing of results is also more sophisticated and much more time-consuming. In most demanding cases, with meshes up to $10^8 - 10^9$ cells, the storage capacity and I/O overhead becomes the limiting factor, with simulations evolving towards the concept of a numerical wind tunnel (the results are reliable but not all the data can be stored for analysis) [7]. This requires an aprioristic definition of the post-processing, with a predefined strategy to only write the processed data and update statistics on the run.

Latest contributions in the open literature to LES modeling of multistage turbomachinery include simulation of gas turbine compressors at off-design conditions [10], high-pressure turbine stages with blade/vane rescaling [11],[12], high-pressure turbine blades [13] or fan modeling in a turbofan [14]. In the case of tip-leakage modeling, the grid requirements are dramatically increased, up to 10^7 to $2 \cdot 10^7$ cells for wall-modeled computations and even 10^8 to $2 \cdot 10^8$ cells when wall-resolving meshes are employed. All these examples include very complex physics like laminar-to-turbulent transitions, heat transfer, shock waves, swirling flow or detached and secondary flows, so an extremely high number of cells is mandatory. When end-wall flows with tip vortices are not modeled for the isothermal flow in the mid-span region of a low-speed fan, the complexity is considerably reduced and the number of grid points can be significantly relaxed. In this work, a numerical simulation of the flow inside a single-stage, low-speed axial fan in a Rotor-Stator (R-S) configuration is performed using wall-modeled LES computations. This numerical approach allows an accurate description of the turbulent wakes and their interaction with downstream rows, especially at off-design conditions and despite the geometrical simplifications adopted. In particular, the blade/vane rescaling and the analysis of the midspan section (a total span of a 12% of the blade chord), combined with the isothermal, low-speed aerodynamics of the fan stage, have allowed the use of a moderate mesh density for a prospective model with LES computations of a subsonic industrial fan. Both temporal and spatial discretizations have been carefully selected for economy and computations have been performed according to standard requirements for a wall-modeled LES with reasonable CPU times [15].
Phase-averaging techniques have been employed to both resolved and modeled variables in order to obtain a complete description of the turbulent scales. These techniques provide a whole picture of the kinetic energy budget of the flow, which also allows to validate the length of the LES filter. The definition of the numerical methodology is completed providing a thorough analysis of the ensemble-averaging characteristics to obtain a statistically accurate description of the flow. The guidelines proposed (and contrasted) allow to minimize the typical long runs required in LES for obtaining representative enough time-resolved results. In essence, the required number of ensembles for a given convergence threshold may be determined a priori if a rough estimation of the mean-time (background) turbulence level is known.
Additionally, a significant effort has been made to validate the analysis of the numerical results with previous published experimental data from the authors [16],[17]. Meantime and phase-averaged distributions of velocity and turbulent kinetic energy at the stage exit have been compared with hot-wire measurements of the real fan geometry. In those regions where the flow is primary planar (without radial migration of momentum and free of shroud end-wall effects), LES evidences for massive separation at reduced frequencies in the outlet vanes are experimentally confirmed. The detailed description of the flow for different operating conditions and the superior ability of LES computations to simulate blade-wake and wake-wake interactions with highly-vortical, detached flow is clearly demonstrated.

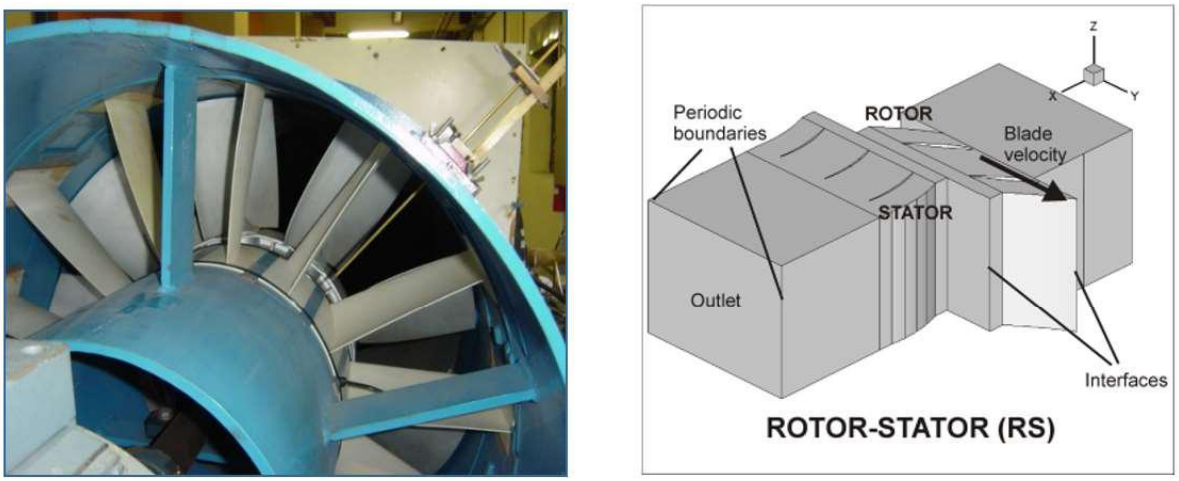

Figure 1: Axial fan (left). 3D geometry of the axial cascade (right, unscaled)

2. Numerical methodology and LES computations

2.1. Rotor-stator model

The turbomachine under study is a single-stage low-speed axial fan with a classic R-S configuration (Figure 1, left). The fan is composed by a 9-blade rotor, based on the NACA 65-012 class and a 13-vane stator based on the British circular profile C1. The hub and tip diameters of the machine are 380 and 820 mm respectively, with a nominal distance for the axial gap between the rows of 50 mm. The rotational speed is 2400 rpm with a design flow rate of 18 m^3/s and a total-to-total pressure rise of 1.2 kPa. To analyze the behavior of the machine at different operating conditions, three different flow rates have been analyzed for each configuration: nominal flow rate (Q_N), partial load (85% Q_N) and near-stall conditions (70% Q_N). More details can be found in [17] .
In the present study, only results concerning the spanwise sections, where the bulk flow is away from solid boundaries and the radial components are negligible (approx. between 60 and 70% of the span), have been considered. Thus, all the effects linked to the presence of the hub and shroud end-walls have been neglected, focusing on the R-S interaction only. Centrifugal forces have not been considered, according to the radial equilibrium imposed by the free-vortex design of the fan blades. All these premises allowed the reduction of the computational model to a 3D extruded linear cascade. On the basis of kinetic geometrical parameters, the corresponding 2D section was extruded spanwise for one tenth of the blade chord to perform fully 3D computations. This artificial rigid extrusion was adopted to preserve the 3D vortical nature of vortex shedding in the lattice of wakes throughout the stage.

2.2. Numerical scheme

The commercial CFD software FLUENT® was used to solve the Navier-Stokes set of equations in an incompressible fashion, introducing an unsteady 3D viscous scheme for the finite volume method, with second-order accuracy

for the temporal discretization. A third-order MUSCL formulation has been employed for the convection terms, which improves, compared to the second-order upwind scheme, the spatial accuracy for all types of meshes by reducing numerical diffusion, especially for complex three-dimensional flows. The diffusion terms are central-differenced and second-order accurate. In addition, the turbulence closure is addressed using a LES scheme, which solves directly the large scales of the flow, but models the effect of eddies smaller than the grid cell size. In the case of turbomachinery, with typical high Reynolds numbers, it is important to rely on an appropriate model for these scales [18]. A subgrid scale model is introduced after filtering the incompressible Navier-Stokes equations (in the following, a hat denotes a subgrid average).

- Continuity equation:

$$\frac{\partial \hat{u}_i}{\partial x_i} = 0 \tag{1}$$

- Momentum equation:

$$\rho \frac{\partial \hat{u}_i}{\partial t} + \rho \frac{\partial \left(\hat{u}_i \hat{u}_j\right)}{\partial x_j} = -\frac{\partial \hat{p}}{\partial x_i} + \mu \nabla^2 \hat{u}_i + \frac{\partial \tau_{ij}}{\partial x_j} \tag{2}$$

where $\tau_{ij} = -\rho\left(\widehat{u_i u_j} - \hat{u}_i \hat{u}_j\right)$ is the subgrid scale stress tensor. This tensor is modeled via the Smagorinsky-Lilly closure model:

$$\tau_{ij} = 2\nu_T \hat{S}_{ij} \tag{3}$$

$$\nu_T = L_S^2 |\hat{S}| = \left(C_S \hat{\Delta}\right)^2 |\hat{S}| \tag{4}$$

where L_S is the mixing length for subgrid scales, ν_T is the subgrid eddy viscosity, C_S is the Smagorinsky constant (0.1 in our case), $\hat{\Delta}$ is the local grid size, S_{ij} is the resolved scale strain rate tensor and $|\hat{S}| = \sqrt{2\hat{S}_{ij}\hat{S}_{ij}}$.
The Smagorinsky SGS model is the simplest and most robust closure to be used in LES computations of turbomachinery. Although recent investigations have revealed that it may present dissipative characteristics, especially for shock flow structures, it can still provide a good prediction of the important flow patterns and even an accurate reproduction of secondary flow features [11]. Hence, a wide number of researchers are still relying on this SGS model for their LES computations in rotor/stator stages due to its simplicity and versatility [12], [13], [10].

2.2.1. Geometry and boundary conditions

The boundary conditions implemented in the numerical model are shown in Figure 1, right. Translational periodicities have been introduced in both rotor and stator zones to impose tangential repeatability and avoid a complete discretization (i.e., a full-annulus model). With a real vane-to-blade count ratio of 13:9, a circumferential approximation has been adopted to reduce the

periodicity to a simplified 3:2 ratio, so just 3 vane passages and 2 rotor passages were modeled for the full unsteady computations. The necessary pitch modification of the stator vane row is around 3%, which has been considered negligible for this kind of turbomachines [19]. Figure 1 also shows the moving planes (interfaces) that allow the relative displacement between the rotor and stator domains. A constant inflow velocity has been set as the inlet boundary condition for the computations, with a typical value of inlet turbulence (around 1.5%) and a characteristic turbulent length scale of $\ell_0 = 0.13$ m, a fraction of the casing diameter (data obtained from previous experimental measurements for this type of turbomachinery [20]). The velocity condition of the incoming flow in LES cannot be directly specified due to the random nature of the flow. Therefore, it is necessary to produce a perturbation in the initial flow field and the incoming flow [21]. This generation of turbulence at the inlet is achieved using a spectral synthesizer included in FLUENT®, which calculates fluctuating velocity components by synthesizing a divergence-free velocity-vector field from the summation of Fourier harmonics. At the exit surface, an outlet pressure boundary condition has been set ($p_{atm} = 0$), and top and bottom surfaces have been considered as frictionless walls. The computational domain has been extended several chords upstream and downstream of the stages to avoid any unrealistic effects from inlet or outlet boundary conditions on the flow.

2.2.2. Computational mesh

LES techniques are still unaffordable for shear flows with wall contours and moderate to high Reynolds numbers, so near-wall regions must be treated with a special formulation. With this aim, the mixing length for subgrid scales is calculated as follows:

$$L_S = \min\left(\kappa d, C_S\hat{\Delta}\right) \tag{5}$$

where κ is the von Karman constant, d is the distance to the nearest wall and C_S and $\hat{\Delta}$ are the same defined in Equation 4. The local grid size is computed as the cube root of the computational cell volume:

$$\hat{\Delta} = V^{\frac{1}{3}} \tag{6}$$

In this way, the definitive WMLES formulation is completed as:

$$\nu_T = f_D \min\left(\kappa d, C_S\hat{\Delta}\right)^2 |\hat{S}| \tag{7}$$

being f_D a near-wall damping function.

Due to the different tangential pitches of the stator and rotor passages, it is necessary to employ a non-conformal mesh. In addition, the grid density has been fixed according to the minimum requirements needed to complete an accurate wall-modeled LES (WMLES) simulation [6]: $\Delta x^+ = 100 - 600, \Delta y^+ = 20 - 150, \Delta z^+ = 100 - 300$, which for a structured, equally-spaced grid is equivalent to a given number of nodes in the boundary layer thickness [5]:

$$N_x \approx \frac{\delta}{\Delta x} \approx 10 \tag{8}$$

$$N_y \approx 30 - 40 \tag{9}$$

$$N_x \approx \frac{\delta}{\Delta z} \approx 20 \tag{10}$$

where N_x, N_y and N_z are the number of cells per boundary layer thickness δ in the streamwise, wall normal and spanwise directions respectively.
For both blade and vane surfaces, a typical O-grid distribution with a [100x60] mesh density was employed to discretize the boundary layers. This number of nodes is consistent with the recommendations available in the literature [9], [22], suggesting around 1500 nodes necessary for a δ^3 outer volume in the $y^+ > 100$ region. Lieblein correlations [23] for NACA 65-(A10) blades have been used to estimate a characteristic size around $\delta = 12.5$ mm for the boundary layer thickness near the TE, so the average cell size in the vicinity of vanes and blades resulted in $\Delta_{cell} \sim \delta/N^{1/3} = 12.5/1500^{0.33} = 1.12$ mm. In the normal direction the restrictions are stricter so a progressive structured mesh was employed with the first grid point placed at 0.05 mm from the wall. In the z-coordinate, the spanwise direction was covered with 15 cells, for a total height of the model of 0.12 blade chords, following the guidelines by Davidson and Dählstrom [15]. The total number of 120,000 cells employed in the model for the blade surfaces is also consistent with the correlation given by [8] for the number of nodes required for the outer layer of turbomachinery boundary layers: $N = 3000(w/c)Re^{0.4}$, where w/c is the ratio between the blade span and its chord and Re is the Reynolds number on the blades based on the chord length. In this case, $w/c = 0.12$ and $Re = 8.5 \cdot 10^5$, so the estimated number of cells required for the outer layer is around 85,000 cells.
In addition, the mesh density within the passages has been carefully selected in order to capture vortical structures in the range of the integral length scales when large separation arises (i.e., rotor wake at near-stall conditions). If this average cell size of the outer BL is maintained for the whole blade passage (around 1 mm, with dimensions 210 mm (pitch), 165 mm (chord) and 19.8 mm (reduced span), the required number of cells in the mid-passage of the blades is $N = 210 \cdot 165 \cdot 19.8/1.123 \sim 490,000$ cells. As a consequence, adding the number of cells in the boundary layer, the total number of cells per passage should be around 610,000 cells, leading up to 3.05 million cells for the whole domain (5 passages) which is in total agreement with the current grid of the model (3.4 M cells). Moreover, previous experimental investigations by the authors in this family of axial fans have determined that typical sizes around 2 mm are needed rotor downstream to describe the largest eddies at midspan locations [24], which is also in accordance with the theoretical estimations. Figure 2 shows a detail of the mesh in the vicinity of the rotor blades leading edge (B) and stator vanes trailing edge (V) respectively.

2.2.3. LES modeling and resolved scales

The sliding mesh technique has been employed in the simulations to reproduce the relative movement of the rotor blades with respect to the stator vanes.

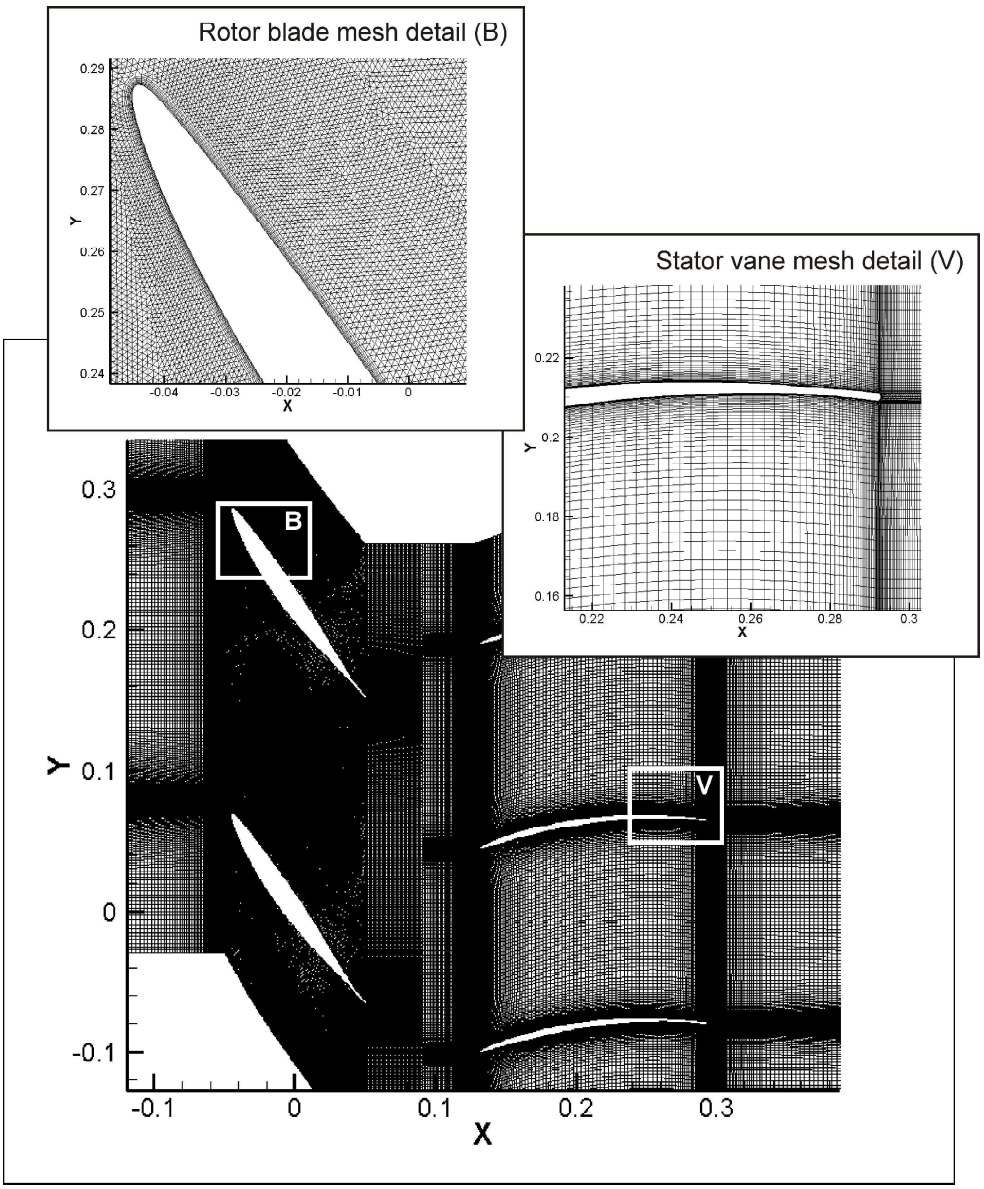

Figure 2: Mesh topology and grid details (Fernández Oro, et al., 2012)

For that purpose, two independent meshes had to be defined in the model, sharing a common interface zone where the information is exchanged. In the stator, the equations are solved in an absolute reference frame, while in the rotor they are solved in a relative domain. In addition, the numerical routine is executed unsteadily: the impeller mesh is moved tangentially at every time step, changing the relative position of the rotor blades with respect to the stator vanes. To quantify the dissipation rates of the flow variables along the rotor-stator interface, the error in the transmission of the instantaneous axial velocity between the interfaces in the fixed and rotating domains has been obtained. In particular, the meantime value of the error has been computed and averaged spanwisely in the relative frame of reference for the different operating conditions (see Figure 3). The highest instantaneous errors are associated to the convection of the rotor wakes, as evidenced in the plot, with maximum errors up to 4% for all the working points. These percentages are considered assumable for the objectives

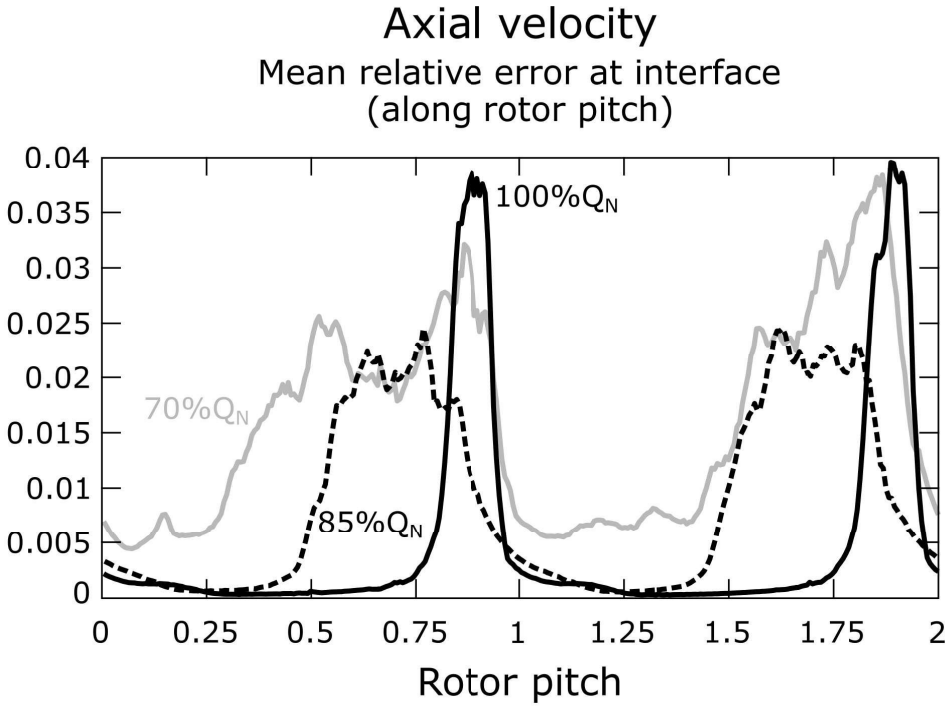

Figure 3: Spanwise-averaged conservation of properties at the interface in the rotor frame for different flow rate conditions

of the present investigation.

A gradual solution procedure was executed to ensure stable convergence, following the guidelines proposed in [25]. Basically, a steady solution using first order schemes is initially resolved to be progressively updated using high-order discretizations in both turbulent transport equations and momentum balances. For this new work, a final stage executes a full unsteady simulation with the LES technique and a classical Smagorinsky-Lilly model for the closure of the subgrid turbulent stresses. LES computations are extended for several through-flow intervals in order to guarantee that the flow is well established inside the passages. More details about the number of executions required is given in Section 3.

Additionally, the selection of an appropriate temporal resolution to resolve the turn-out time of the resolved eddies in the LES scheme is also critical. In the present case, a temporal time step of $9.26 \cdot 10^{-5}$ s, equivalent to 30 intermediate time steps per blade event, has been fixed. To validate this selection, Figure 4 shows the power spectrum density of several instantaneous velocity signals measured with hot-wire anemometry and computed at half a chord downstream of the rotor blade for the RS configuration. Peak values in the spectra correspond to the Blade Passing Frequency (BPF) and its harmonics. The solid black line represents the experimental spectrum, while blue, green, red and grey lines show numerical results computed with different time steps. As the number of time steps per blade event is progressively reduced, there is an evident lack of accuracy in the spectra of the time series. From the comparison of the energy content (the area under the curves) of the numerical and experimental

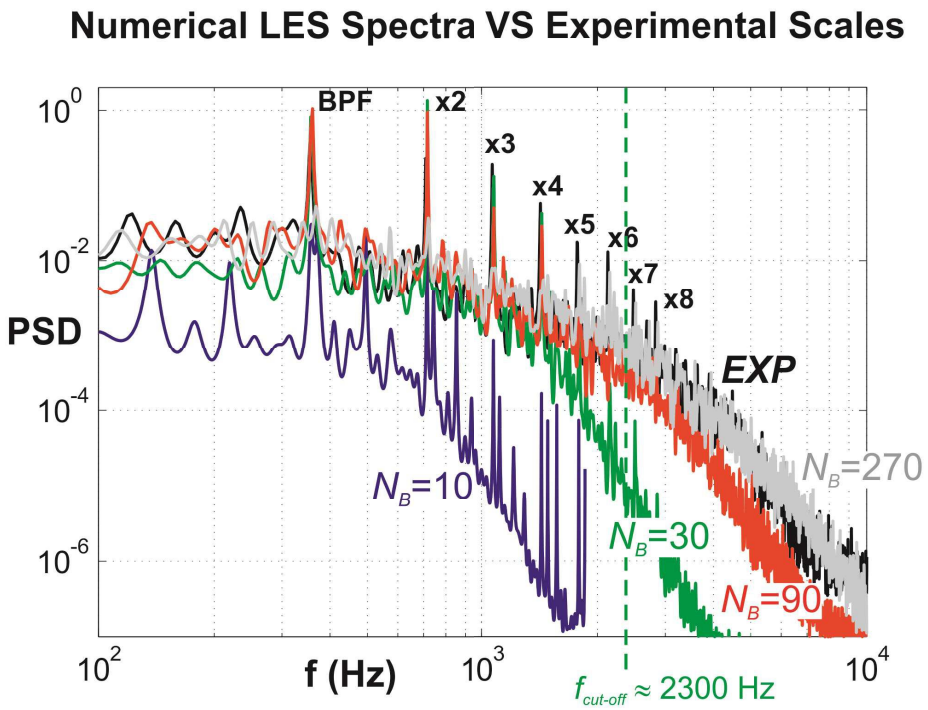

Figure 4: Accuracy of LES computations as a function of time step.

spectra, it is derived that nearly 270 time steps per blade event are required to resolve close to 95% of the turbulent kinetic energy, while 90 time steps account for roughly 85%. However, a moderate choice with 30 time steps was found to be reliable in terms of the turbulent energy resolved by the numerical model. With almost 70% of resolved turbulent budget, this was considered sufficient for economy. With this selection, the cut-off frequency of the LES filter is placed at $\pi/\Delta_{cell} \approx 2.3kHz$ (see green dashed line in Figure 4). For the present numerical mesh, $\Delta_{cell} \sim (\Delta x \Delta y \Delta z)^{1/3}$ is around 1.37 mm at the measurement point, in the range of the cell size discussed above. This implies that eddy sizes smaller than $\ell_c \sim 2\pi/f_{cut-off} \approx 2\pi/2300 = 2.75mm$ are filtered out in the computations. However, since local integral length scales are found to be in the order of 20 mm [24], it can be assumed that this temporal discretization for our LES computations still provides a valuable description of the largest turbulent scales of the rotor wakes.

2.3. LES computational requirements

Regarding the computational cost, all the calculations presented have been executed on a home-made cluster, consisting of four parallelized quad-core PCs at 2.67 GHz with 4 GB of RAM in each node.
Initially, simulations were performed during 600 time steps for every case. Considering 30 time steps per blade passing period, this implied the storage of 20 blade events for ensemble averaging. However, the analysis of preliminary results showed that the level of convergence was clearly insufficient with this selection. As a consequence, it was decided to increase the simulation time an

order of magnitude, so finally all the cases were studied using 6600 time steps. This choice generated 7.2 GB of numerical information per case to be post-processed.
The huge computational requirements needed for this type of numerical methodologies are evident from the total CPU time employed in each of the three cases analyzed: up to 450 hours to simulate 200 blade passing-periods, i.e. 25 rotor turns for a converged statistical description of the unsteady flow patterns.

3. Post-processing and data identification techniques

3.1. Post-processing procedure

The analysis of instantaneous velocities and subgrid turbulent viscosities for three operating conditions has been performed, monitoring and averaging the data in a planar window in the fixed domain. The streamwise extension of the window is equivalent to five chords of the stator vanes, whereas the tangential width is kept to three stator vane pitches. This corresponds to more than 40,000 points of numerical information.
In the present investigation, the results concerning the stability and turbulent characteristics of the flow within the outlet region of the fan (stator downstream) are presented in detail below. These locations represent the zones with higher interaction between viscous phenomena (wake-wake interaction), susceptible for higher instability due to the inherent disorder of the shear layers.
Matlab® software was used for data processing, due to its powerful treatment of variables in a matrix arrangement. A post-processing home-made code allowed reading data from FLUENT® files, running averages to filter turbulent scales and blade passing phenomena, interpolating to prevent data from patchiness and plotting maps and distributions to present the final results in the zones of interest. The execution of all the numerical routines in Matlab® also represented a significant computational load. Particularly, the completion of the ensemble-averaging required approximately 50 hours of CPU time (in a single PC) for every studied case.

3.2. Data identification techniques

The segregation between unsteady deterministic features and turbulent scales is essential to understand the unsteady mechanisms responsible for energy transfer in turbomachines. This requires an accurate selection of the temporal resolution and the number of blade passing periods to be monitored to ensure a valid statistical reduction.

3.2.1. Ensemble & time-averaging

Ensemble-averaged values in turbomachinery environments are computed by isolating a number of blade passages (i.e., 220 events in our database), dividing them into a fixed number of classes (i.e., 30 time steps), and making averages among the corresponding classes. With this average, chaotic flow variations can be eliminated obtaining the unsteady deterministic field. Following, the

unsteady flow structures can be filtered out using a further time averaging, so fluctuations due to the periodic passing of blades are removed and a final steady flow pattern is recovered.
Considering periodicity between consecutive rotor blades, the phase- or ensemble-averaged value of a trace velocity component u at the time or phase n (angular position) is obtained as:

$$\tilde{u}_n^{(M)} = \frac{1}{M} \sum_{m=1}^{M} u_n^{(m)} \tag{11}$$

where the subscript n represents the n-th angular position of the measured trace and the superscript (M) indicates that the ensemble-averaging has been completed using M realizations. The superscript tilde symbol represents the ensemble-averaging.
Additionally, non-deterministic scales (turbulence) are directly obtained subtracting the time-resolved (or phase-resolved) velocity defined in Equation 11 from the original, instantaneous trace, according to $u'_n = u_n - \tilde{u}_n^{(M)}$. Finally, the time-averaged velocity may be obtained introducing a time-averaging operator that provides its overall (steady) mean value. Here, it is denoted with an overbar.

$$\bar{u} = \frac{1}{N} \sum_{n=1}^{N} \tilde{u}_n^{(M)} \tag{12}$$

The application of this procedure is illustrated in Figure 5, with a non-dimensional representation of the axial velocity for near-stall conditions of the numerical axial cascade. This type of contour map, which will be employed continuously along the paper, shows the flow variables downstream of the vanes for one stator pitch in the transversal direction. An instantaneous snapshot (Figure 5a) is firstly represented with all the turbulence scales superimposed to the unsteady flow. Four different rotor wakes can be roughly identified as they are convected along the stator vane. Two recirculation bubbles are also observed, due to the adverse pressure gradient at low operating conditions. In Figure 5b, the ensemble (or phase) averaged flow is presented at a particular position of the rotor blades (phase $t/T_B = 0.47$), showing a clean flow pattern with smooth rotor wakes (low velocity traces moving tangentially upwards). Finally, the time-averaged flow (Figure 5c) is a meantime, steady map of the flow pattern on the fixed frame of the stator vanes where all the unsteadiness and fluctuations are removed.

3.2.2. Turbulent (subgrid modeled and resolved) and deterministic kinetic energy

Resolved velocity fluctuations, filtered out in the ensemble-averaging process, contribute to a significant part of the turbulent stress tensor if the LES scheme is well-posed. On the other hand, the minor part is modeled (in the addressed subgrid scales) via the subgrid turbulent viscosity of the Smagorinsky-Lilly closure. Previous considerations with experimental validations in the rotor wakes revealed an expected subgrid kinetic energy in the order of a 30% with the time

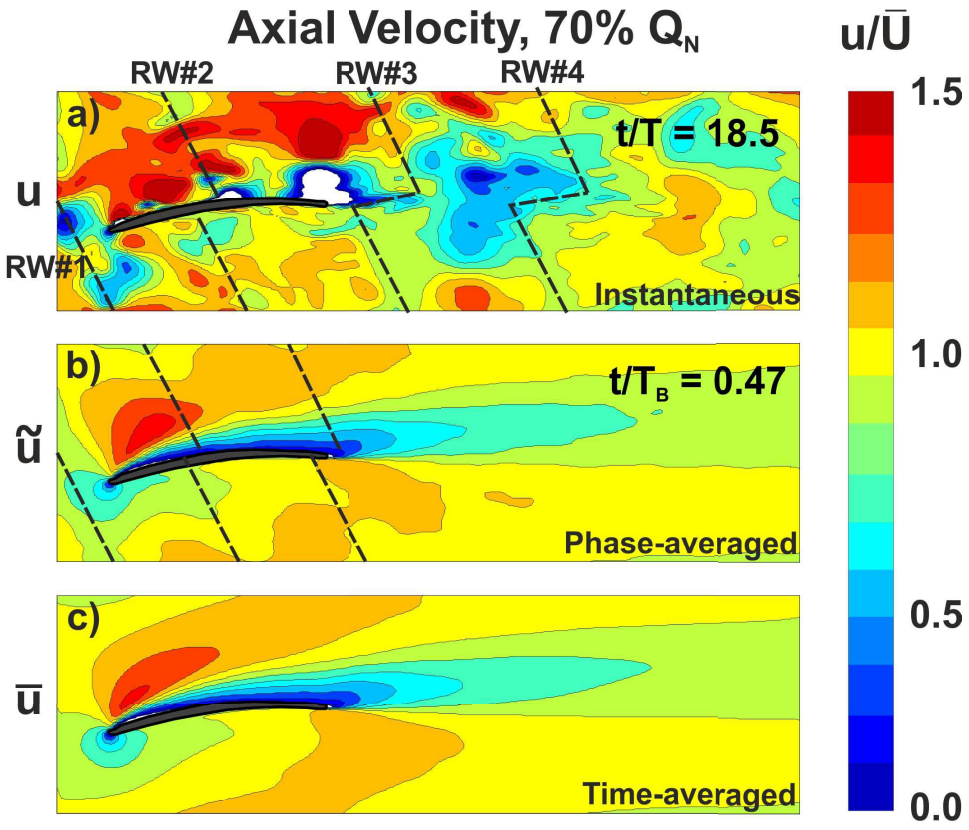

Figure 5: Illustration of ensemble and time-averaging operators.

step employed to generate this database.

In figure 5, the quality of the LES filter in the stator region for the resolved scales is shown. It compares the energy content of both resolved and subgrid (modelled) fluctuations in terms of the kinetic energy (the main diagonal of the turbulent stress tensor). In particular, the phase at which an incoming rotor wake is about to impinge in the stator leading edge at near-stall conditions is analyzed. The high generation of turbulence at the stator vane is perfectly captured with the time-resolved flow (a). Also, the marginal content of the subgrid energy (b) confirms that turbulence production in the suction surface of the vanes is produced at large scales due to the high vortical separation of the flow (note the difference of two orders of magnitude in the colorscale). In addition, Figure 6 includes a table that summarizes the energy content of the largest flow scales for both resolved and subgrid contributions for all the operating conditions studied. Even for nominal conditions, with no massive separations and a high-Reynolds turbulent wake at the stator wake (see Figure 7a), the residual component of the modeled scales is sufficiently small (12.8%).

Additionally, turbulent and deterministic kinetic energies (TKE and DKE) are compared for the whole database in Figure 7. Turbulent and deterministic energies are obtained from the following equations:

$$K_T = \frac{1}{2}\widetilde{u_i' u_i'} \tag{13}$$

$$K_D = \frac{1}{2}u_i'' u_i'' \tag{14}$$

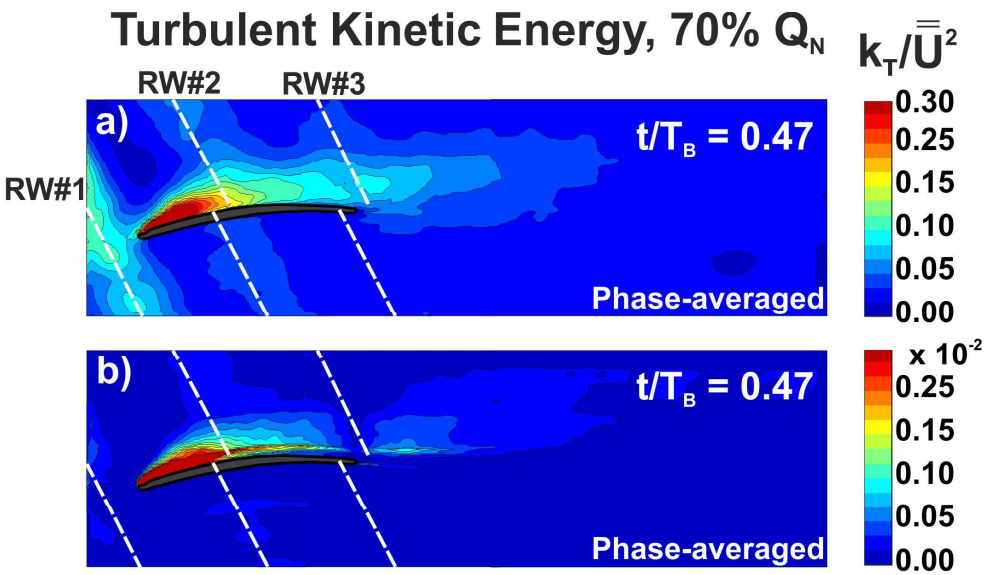

	Flow Rate		
TKE Budget	**100% Q_N**	**85% Q_N**	**70% Q_N**
a) Resolved TKE	32.7	66.9	357.1
b) Subgrid TKE	4.80	8.66	13.58
(%)	**12.8 %**	**11.4 %**	**3.6 %**

Figure 6: Comparison of resolved and subgrid turbulent kinetic energy.

where u_i'' is the ensemble-averaged deterministic fluctuation, defined by $u_i'' = \tilde{u}_i - \bar{u}_i$. The DKE is computed from the unsteady velocity fluctuations generated by the periodic passing of wakes, thus considering only the ensemble-averaged values. In order to compare turbulent and deterministic tensors, it is necessary to perform an ensemble-averaging of the turbulent fluctuations $u_i' u_i'$, as detailed in Equation 13. Finally, a further time-averaging of the resolved turbulent field has been introduced, obtaining the steady maps in the stator frame presented in Figure 7. As it may be appreciated, the maximum turbulent fluctuations double the deterministic ones, due to the tangential movement of deterministic scales for a blade passing period. Deterministic sources are concentrated in the axial gap between the rows, with notably higher R-S interactions for lower flow rates. At nominal conditions, a deterministic spot is observed on the pressure side (PS) of the leading edge of the vanes. Regarding the turbulent kinetic energy, major sources are found in the stator wakes, except for the flow separation in the vanes at near-stall conditions (Figure 7c-left). The existence of phase-averaged turbulent generation in the axial gap due to the circumferential travelling of the rotor wakes at off-design conditions is also noticeable (Figure 7b&c-left). Although the highest R-S interaction (deterministic) it is always perceived on the leading edge of the vanes, it is worth highlighting that, at nominal conditions (Figure 7a-right), this interaction is observed on the PS while at 70% Q_N it is found on the suction side (SS) (Figure 7c-right). Moreover, the SS of the vanes experiences interaction with the rotor wakes only at 85% Q_N, while the fully-detached flow from the vanes at near-stall conditions preserves the region

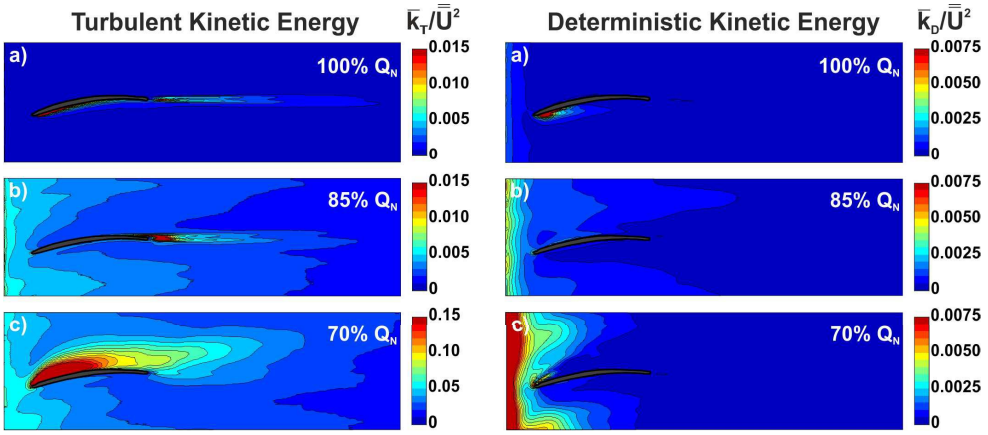

Figure 7: Comparison of mean turbulent and deterministic kinetic energy at different flow rates.

from periodic disturbances.

3.2.3. Assessment of statistical convergence

This section concludes analyzing the number of ensemble averages needed in LES computations to obtain a fully-converged time-resolved flow. All the basic guidelines have been previously discussed in [26] for the experimental measurements from this axial fan. In particular, a statistical indicator of convergence (i.e., a typical residual) is defined as the non-dimensional RMS value of the difference between time-resolved traces using M and M-1 ensembles at every cell of the numerical domain. This definition, always employed in CFD commercial codes for the mathematical convergence of the models, is now redefined to judge physical convergence of the unsteady periodic flow during a blade event:

$$R = \frac{\sqrt{N \sum_{n=1}^{N} \left(\tilde{u}_n^{(M)} - \tilde{u}_n^{(M-1)} \right)^2}}{\sum_{n=1}^{N} \tilde{u}_n^{(M)}} \tag{15}$$

The number of ensemble averages required to obtain a convergence threshold of 10^{-3} (typical in CFD practices) is shown in Figure 8, left, for different operating conditions. Note that this value must be fulfilled for every cell of the stator domain, with the higher turbulent regions requiring a higher number of ensembles to meet convergence. In the case of near-stall conditions (Figure 8c-left), the great generation of turbulence due to flow separation at the vane SS forces a less restrictive criterion for a similar number of ensembles (up to 200). In the right column, maps of the theoretical ensembles for every operating condition are also represented. They are derived from maps of the time averaged turbulence and illustrate the relationship between both variables. This direct correspondence between the required convergence threshold and the local meantime turbulence intensity has been previously demonstrated (see annex in [26]). Note the evident similarities between the post-processed and the theoretical values.
The selection of the convergence threshold is interesting, because it fixes the

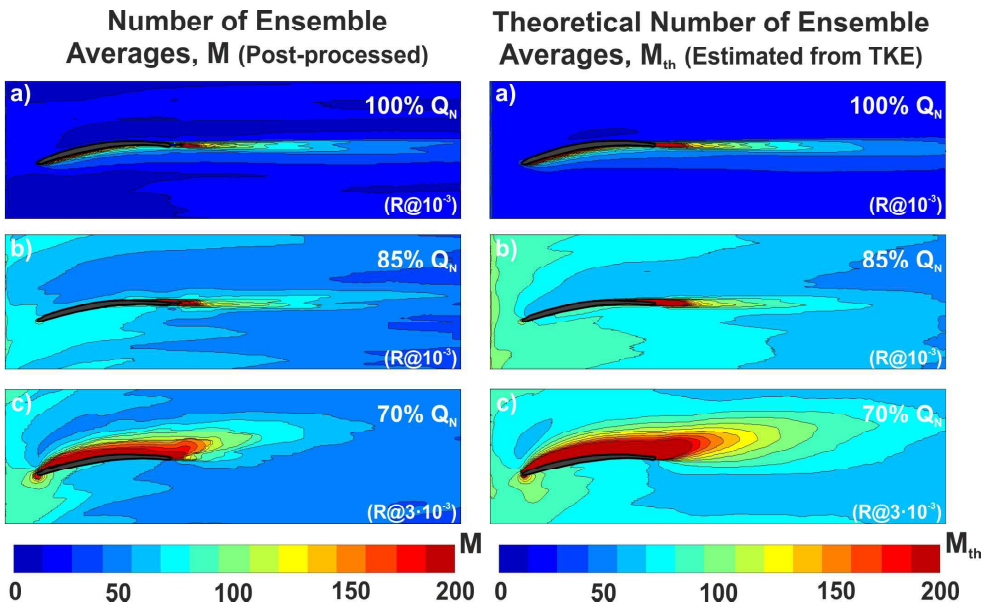

Figure 8: Post-processed and theoretical number of ensemble averages required to ensure statistical convergence at different flow rates.

required number of ensembles and determines the computational cost in terms of total CPU simulation time. A further analysis has been performed to cross-correlate the previous maps in Figure 7 as a function of the residual threshold adopted. In Figure 9, the normalized correlation coefficient has been represented for the three operating conditions, for a residual threshold between $5 \cdot 10^{-4}$ to roughly 100. Maximum values of correlation, close to 0.9, are found in the range between 10^{-2} and 10^{-3}, dropping when moving towards lower residual thresholds due to the limitation in the maximum number of ensembles (200 max.). However, for 70% Q_N (gray triangles), due to the higher levels of turbulence, the correlation factor drops even earlier.

4. Experimental validation

A significant effort has been made in terms of experimental validation to improve the quality of the forthcoming analysis of the numerical results. Dual hot-wire anemometry has been employed intensively to obtain the time-resolved flow in the stator passages. Details of the experimental routines and the overall accuracy of the statistical procedures may be found in [16] and [26]. Special care has been devoted to relating the experimental measurements from the real 3D axial fan and the extruded radial numerical domain in a linear cascade. The relevant similarities in time-resolved and meantime representations between both methods are shown. In addition, the common mechanisms involved in the R-S interaction are highlighted and described as a function of the working conditions in the following subsections.

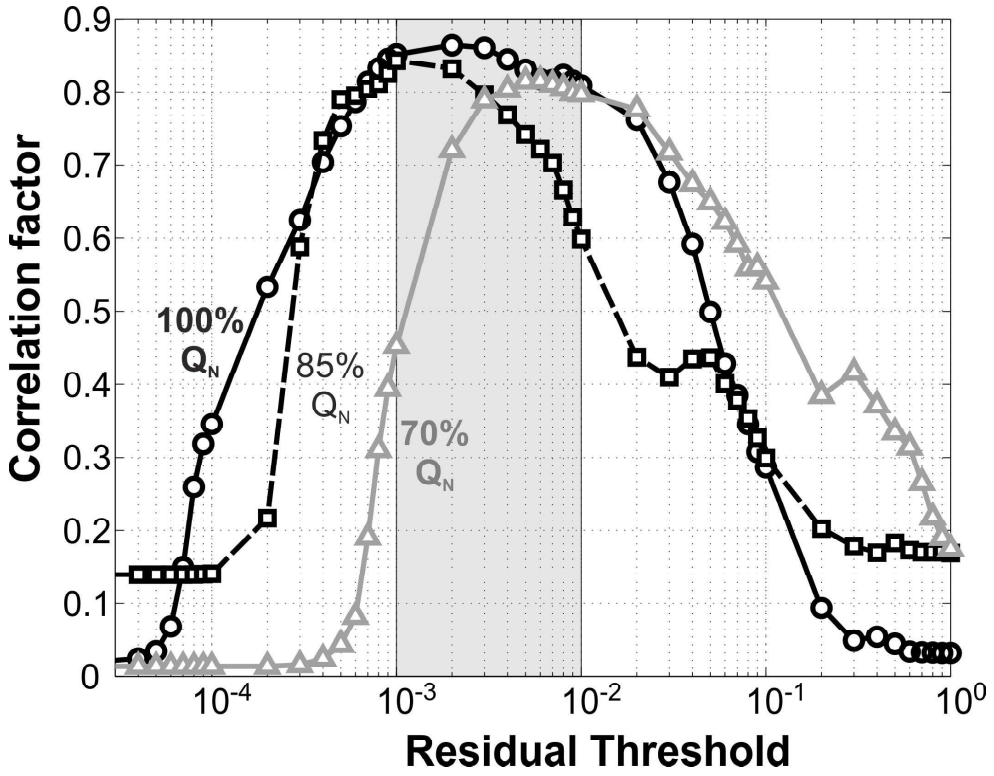

Figure 9: Cross-correlation coefficient between post-processed and theoretical number of ensembles as a function of the convergence threshold for the flow rates studied.

4.1. Local velocity and turbulent kinetic energy traces

Time-averaged representations of the non-dimensional axial velocity for three consecutive stator vanes (three stator pitches) are represented in Figure 10 (top) for both numerical (blue lines) and experimental (red circles) results. They have been evaluated downstream of the stator trailing edge, at one quarter of the chord for all the operating conditions. The meantime velocity deficits of the stator wakes and the progressive widening of the wake-jet structure have been accurately predicted. Moreover, temporal evolutions of the unmixed rotor wakes are also well modeled, as demonstrated by the velocity traces at point B (Figure 10, bottom). Experimental results exhibit a higher level of oscillations, with a more diffused blade-to-blade pattern, being the 85% Q_N the case with the best agreement. Levels of unsteadiness have been found to be 3.7, 6.7 and 5.9% of the mean through-flow velocity for each operating condition.
In addition, the periodic passing of time-resolved TKE at point B is shown in Figure 11. As expected, higher levels of turbulence are found as the fan operating point moves further from design conditions, with reasonable resemblance between the hot-wire measurements and the LES computations. Superimposed small-scales disturbances are preserved in experimental results due to the elementary characteristics of the ensemble-averaging, while they are concealed in LES results due to the filter size. Obviously, all TKE values stator downstream are above the background turbulence level of the experimental facility, a ducted-axial fan with an inlet turbulence of roughly 5%.

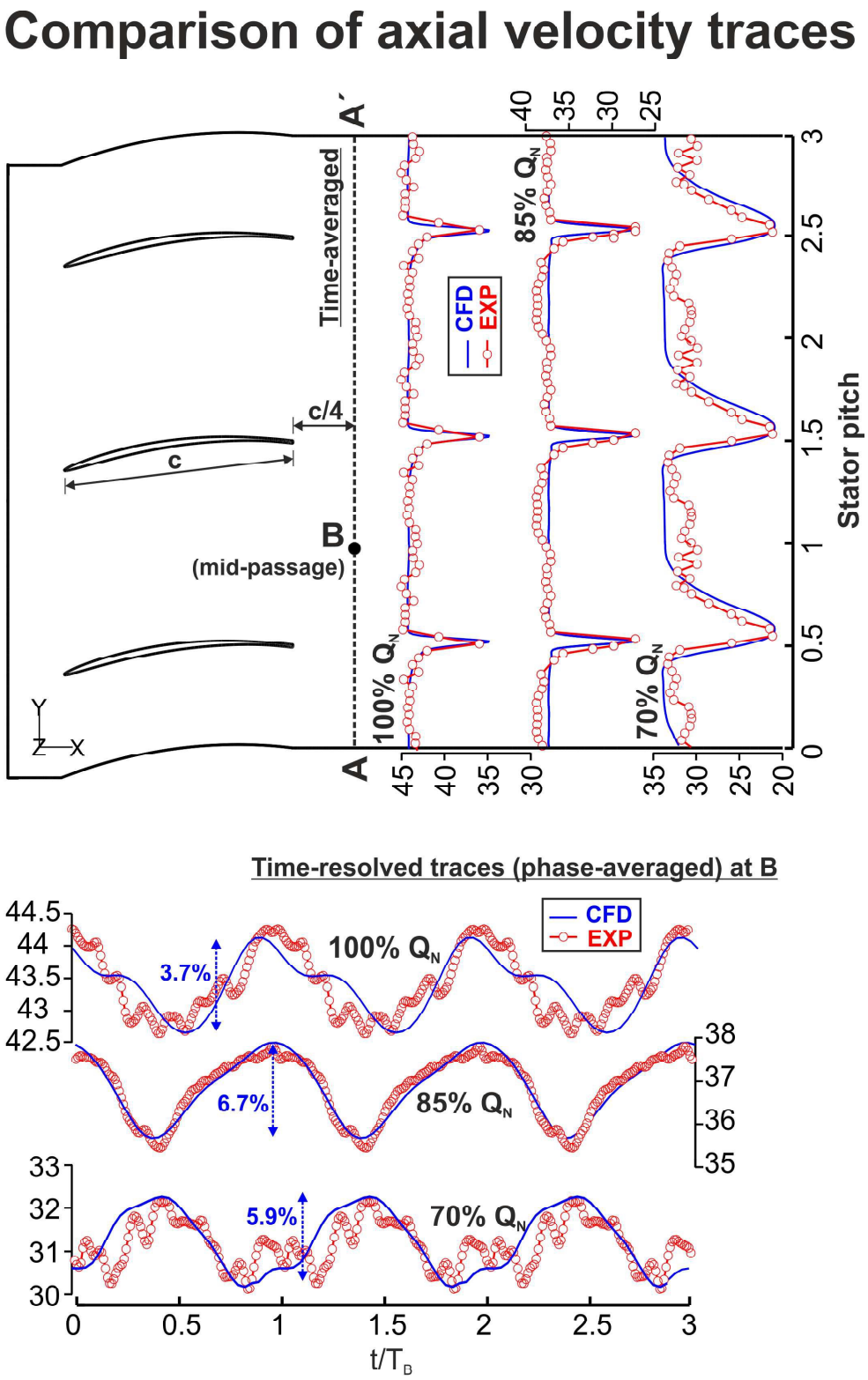

Figure 10: Comparison of experimental (red circles) and numerical velocity traces (blue lines) for different flow rates. Meantime stator flow structures at line A-A'(top). Time-resolved (deterministic) traces at B for three consecutive blade events.

4.2. Time-resolved flow at the stator exit

A deeper insight for validation is performed at the intersection line (dashed line in Figure 12 top, representing the planar flow section at 70% span) between the experimental database (vane-to-vane sector) and the numerical model

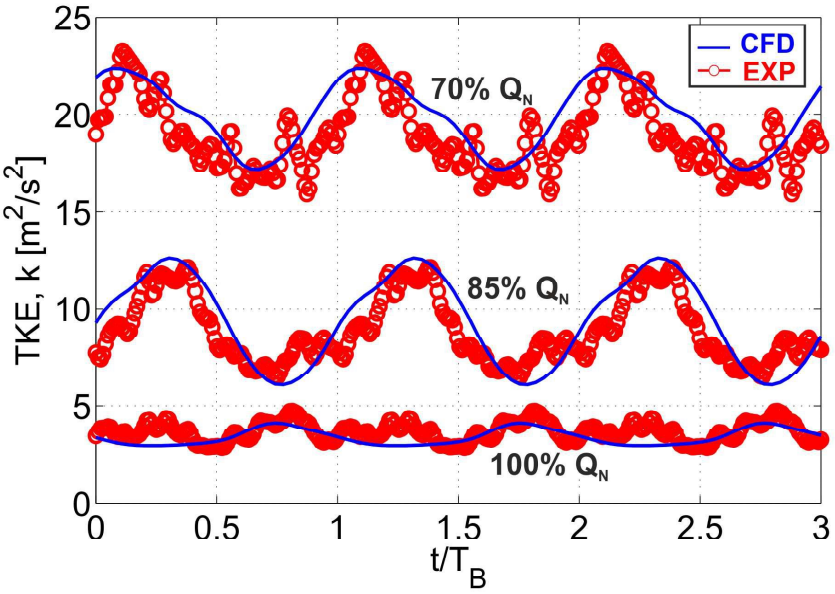

Background turbulence	Flow Rate		
	100% Q_N	85% Q_N	70% Q_N
Inlet TKE (exp.)	6.9	4.6	3.3
Turbulence level	4.94%	4.74%	4.87%

Figure 11: Comparison of experimental (red circles) and numerical turbulent kinetic energy (blue lines) for different flow rates. Time-resolved (deterministic) traces at B for three consecutive blade events.

(vane-to-vane map). The non-dimensional axial velocity for nominal flow conditions is shown in the figure. Time-resolved flow structures at the stator exit are highlighted with a time-space representation of the convection of rotor wakes through the stator passage at Figure 12, bottom. For the sake of clarity, three consecutive periodic blade events have been included. The unmixed rotor wakes (white dashed lines) are tilted and stretched when they interact with the stator wakes. Also, low-velocity regions (yellow spots on the PS) reveal the engrossment of stator wakes due to the periodic passing of rotor wakes. Moreover, a low-velocity region has been found at the stator mid-passage (tangential position of pitch equal to one), coming from a periodic flow detachment from the leading edge of the vanes induced by the impingement of the rotor wakes in the SS. From the comparison of velocity scales and overall flow structures, the accurate description of the viscous R-S interaction provided by the numerical model may be appreciated.

4.3. Instantaneous shedding vortices

To conclude with this validation section, a closer look at the flow characteristics at near-stall conditions is depicted in Figure 13. In this case, two different instantaneous snapshots of the non-dimensional axial velocity are shown in the vane-to-vane map for the computations ($t_1 = t/T_B = 5.77$) and in the transver-

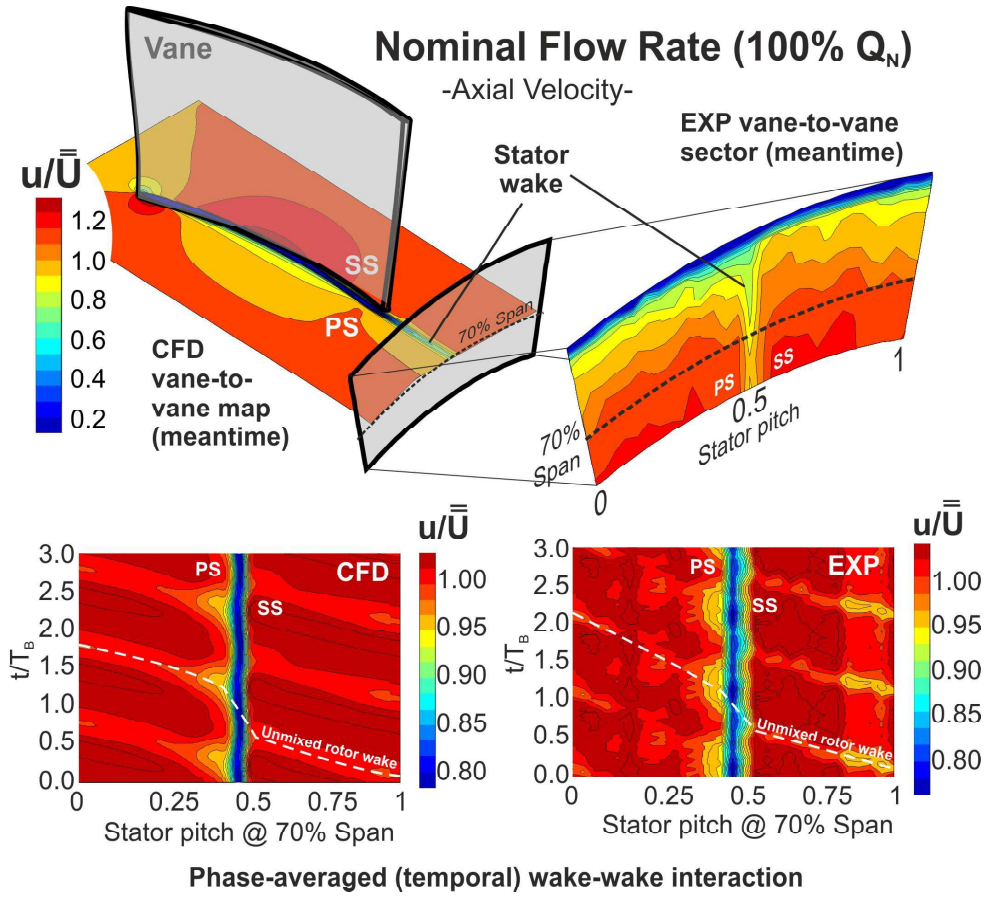

Figure 12: Comparison of time-resolved flow structures at the stator exit: CFD (bottom, left) and experimental results (bottom, right) at nominal conditions.

sal sector for the experiments ($t_2 = t/T = 2.25$). Since the instantaneous flow is represented here, all the turbulent scales are superimposed to the unsteady flow field. Also, the contour maps at the bottom correspond to different time instants, which have been carefully selected to identify the vortex shedding associated to large recirculation bubbles under detachment. The top plots represent the temporal signal of the axial velocity at point C in the experiments (red asterisks) and in the numerical model (blue line). The PSD of the time series is also given aside, with the comparison of the numerical spectrum (blue line) and the experimental ones (raw in black line and with a fifth-order low-pass filter at 1 kHz in red line). The vane downstream region susceptible for detachment is delimited with dashed black lines in the bottom map at the right. A clear path of large recirculation bubbles passes through point C, which can be also identified in the temporal series when large-scale fluctuations of the velocity reduce its non-dimensional value below 0.4. In addition, point C is marked in the experimental results for a corresponding situation of large vortex shedding (left bottom map). A low-velocity spot is identified in the figure as "detached flow" from the SS of the vanes at 70% of the fan span, revealing that these vortical mechanisms have been perfectly captured by the LES computations.

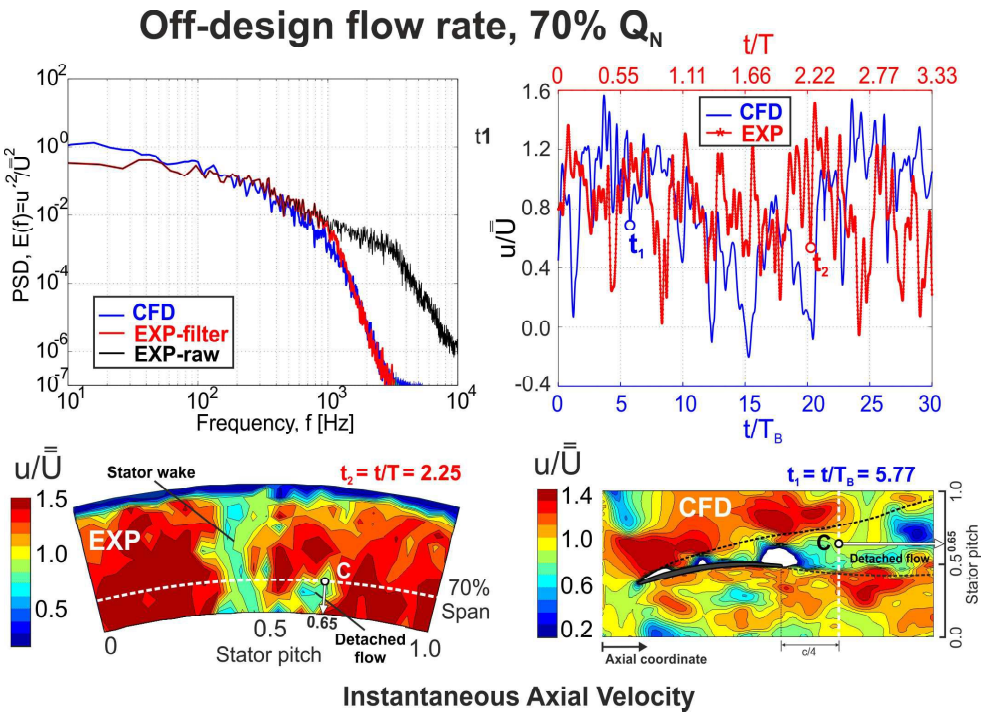

Figure 13: Instantaneous mechanisms of large-scale vortex shedding at near-stall conditions. Comparison of experimental and numerical results.

5. Numerical results

This final section analyzes in detail the numerical results, giving insight on the unsteady and turbulent flow structures in the stator region as a function of the flow rate. The contrasted LES computations are exploited to illustrate the convection of turbulent and vortical structures within the stator passages.

5.1. Time-averaged flow structures

The meantime flow patterns of axial velocity and in-plane vorticity are shown in Figure 14. The axial velocity has been non-dimensionalized with the through-flow velocity of every working point, as previously. The in-plane vorticity has been divided by the rotational speed of the fan. The so-called nominal condition from the rotor reveals a stagnation point on the LE of the vanes and a more extended vane wake than for the intermediate flow rate at 85% Q_N. This suggests the need for a small change in the stagger angle of the vanes to guide the flow and improve the performance of the fan. On the other hand, the large separation observed in the vanes SS at 70% Q_N and the abrupt loss of performance of the vanes from 85% to 70% Q_N indicates that the camber of the vanes is excessive. These evidences can be clearly observed in the representation of both variables in Figure 14.

5.2. Phase-averaged turbulent kinetic energy and pressure coefficient

The phase-averaged turbulent kinetic energy is a suitable variable to visualize the convection of the rotor wakes within the stator passages. Figure 15 (left) shows its temporal evolution on the vanes for nominal conditions. The

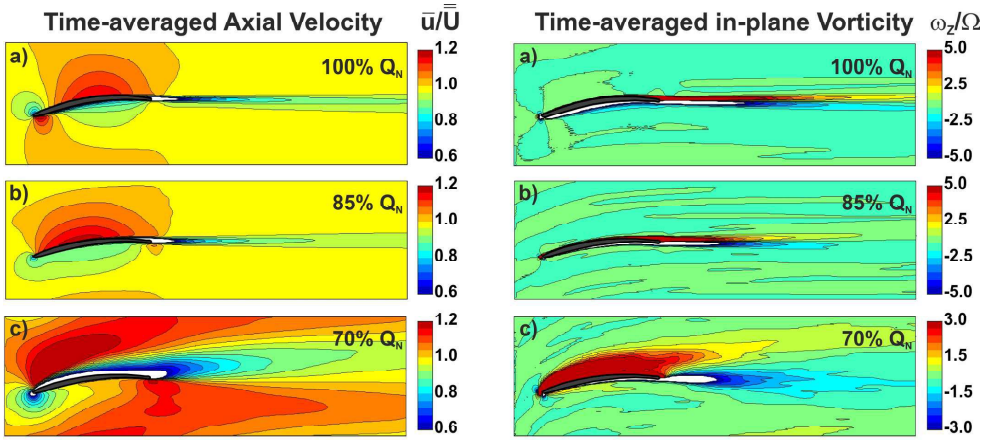

Figure 14: Time-averaged flow structures at different flow rates. Non-dimensional axial velocity (left) and in-plane vorticity (right).

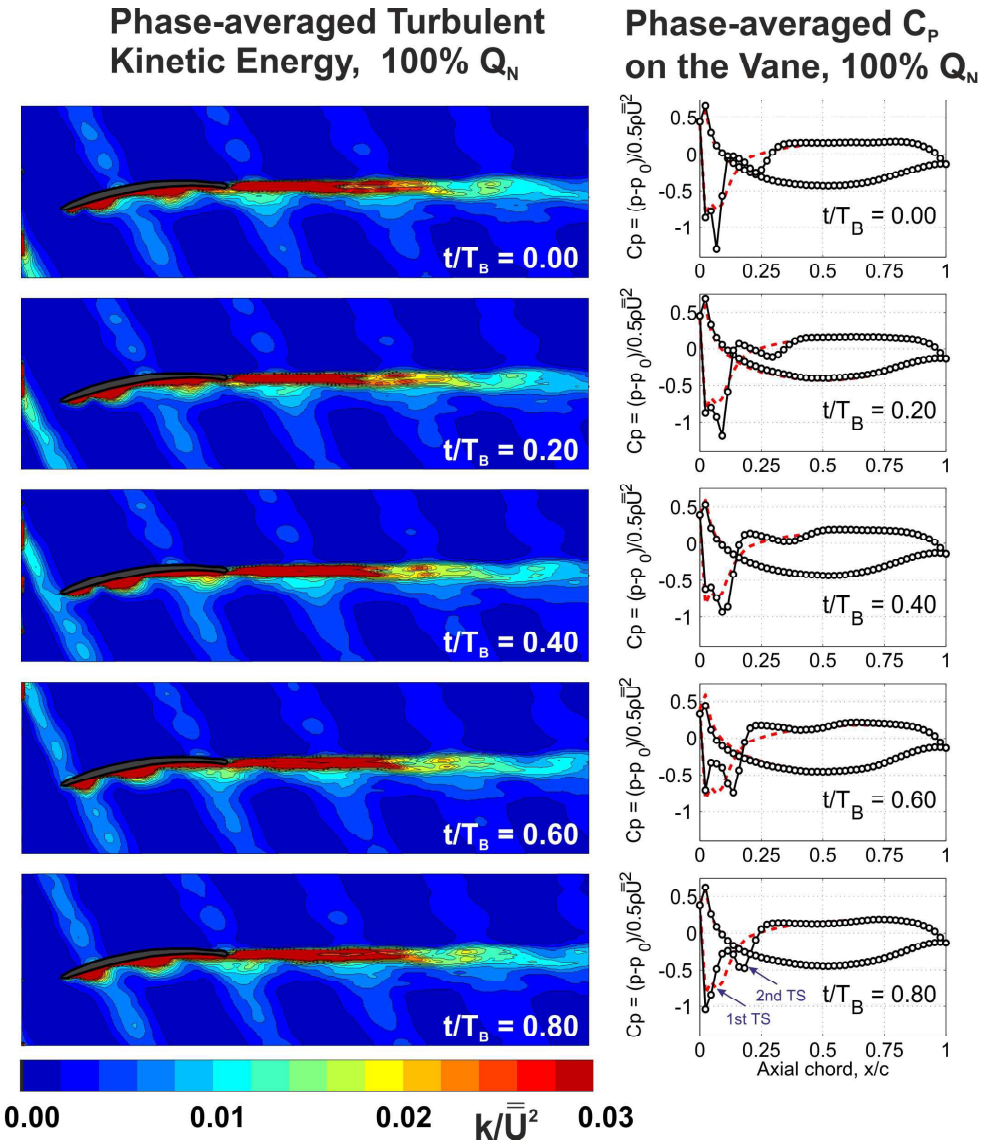

Figure 15: Unsteady convection of rotor wakes through the stator passage at nominal conditions (Q_N). Maps of TKE (left) and distributions of pressure coefficient (right).

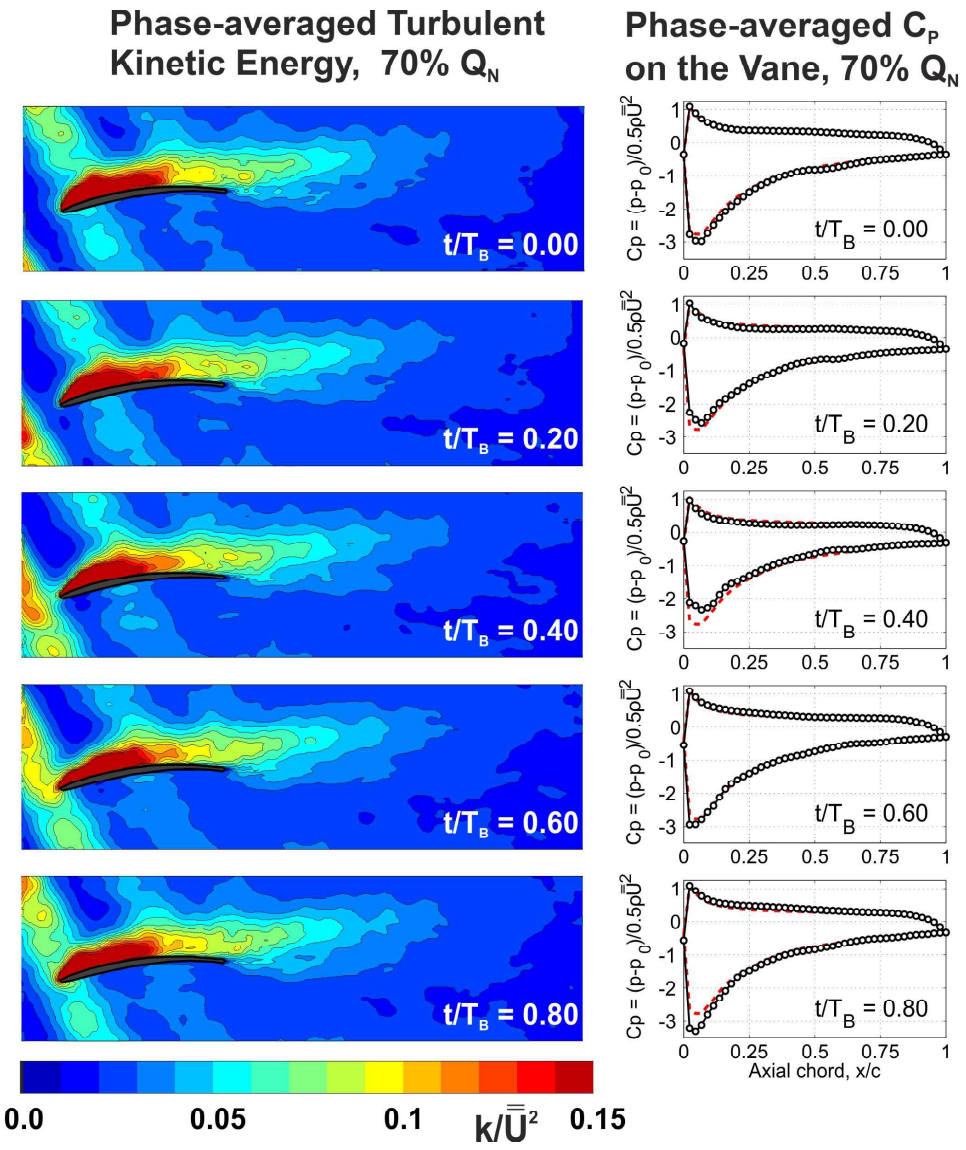

Figure 16: Unsteady convection of rotor wakes through the stator passage at near-stall conditions (70% Q_N). Maps of TKE (left) and distributions of pressure coefficient (right).

impact of the rotor wakes on the generation of turbulence on the pressure side of the vanes is noticeable. A first turbulent spot is found at the LE of the vanes, periodically reinforced by the impingement of the rotor wakes (see for instance $t/T_B = 0.6$). A second region for the generation of turbulence is also observed at mid-chord. In this case, not only are the rotor wakes modifying the intensity of the turbulent spot, but also shifting ($t/T_B = 0.8$) and even chopping ($t/T_B = 0.0 - 0.2$) it along the pressure surface. These mechanisms are also identified in the unsteady distribution of the pressure coefficient, shown in Figure 15-right. The red dashed line represents the mean-time distribution in every plot in order to emphasize the temporal fluctuation for the different rotor phases. The pressure coefficient in the SS remains stable for every temporal instant, whereas turbulent spots induce important pressure drops on the PS.
In the case of near-stall conditions (Figure 16), the large region of detached flow over the suction side of the vanes prevents the impact of the rotor wakes on the stator boundary layer. The pressure coefficient is practically constant over

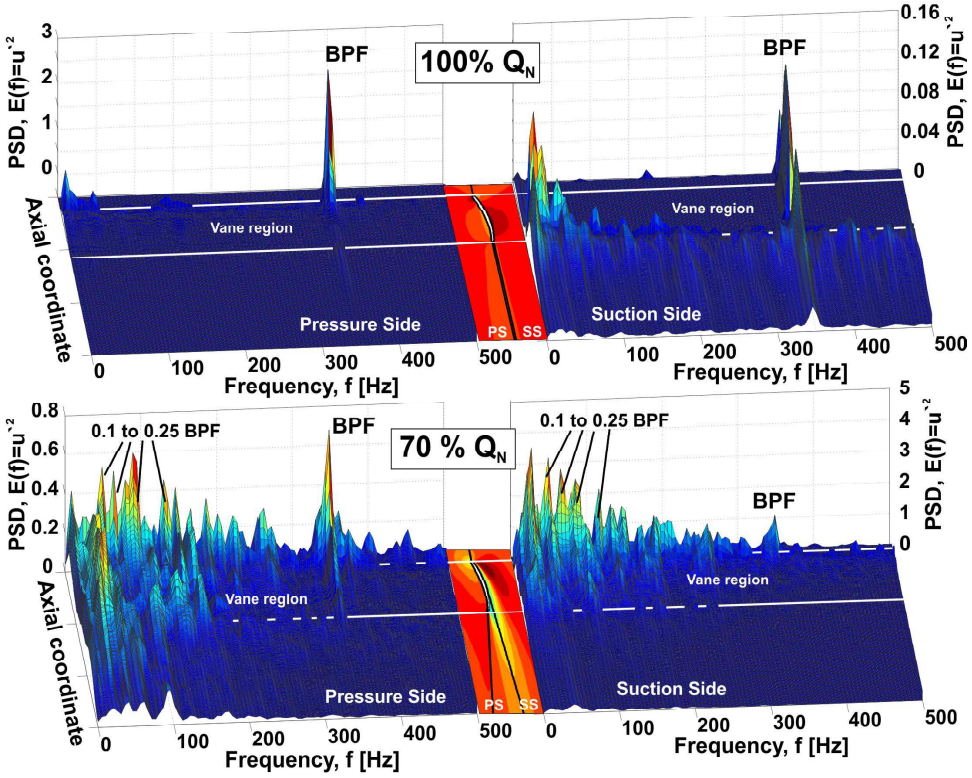

Figure 17: Power Spectrum Densities of the axial velocity on the PS (left) and SS (right) of the vane along the streamwise coordinate. Comparison of nominal (top) and near-stall (bottom) conditions.

time, with only slight fluctuations when the rotor wakes impinge over the vane LE ($t/T_B = 0.8$). Besides, the high overall levels of turbulence in the stator passage induces a quick mixing-out process of the rotor wakes downstream.
More insight into the temporal scales of the vortex shedding associated to turbulence generation in the vane is given in Figure 17. The PSD distributions of the temporal series of axial velocity along the streamwise coordinate for both PS (left) and SS (right) are computed for 100% Q_N (top) and 70% Q_N (bottom) conditions. The paths followed are illustrated in the contour maps of the meantime velocity included between the plots. As expected, the BPF is the main contributor to the unsteadiness of these temporal series. At nominal conditions, the SS reveals low energetic traces (maximum values up to 0.1), being the PS the main contributor to unsteadiness (maximum values up to 2) due to the effect of rotor wakes on the turbulent spots described in Figure 15. At near-stall conditions, this trend is inverted with higher fluctuations levels on the SS of the vanes, with values up to 3. The relevant characteristic is the coherent shedding of large-scale vortices from the vanes at reduced frequencies (between 0.1 to 0.25 of the BPF), which become even more important than the vortices related to the fundamental frequency. On the pressure side, this low-frequency shedding is maintained, but the BPF prevails as the dominant mechanism of unsteadiness.

5.3. Identification of large vortical structures

Movement of larger scales is typically described as vortex-interaction phenomena. Precisely, big vortices arising in turbulent flows, despite their chaotic and random nature, may be identified as coherent structures, i.e. fluid regions that maintain some of their properties for a relatively large spatial and/or temporal extent. Though there are several vortex detection criteria in the open literature [27], the Q-criterion is the most widely used in the case of LES-based simulations. This method defines a vortex as a spatial region where the Euclidean norm of the vorticity tensor dominates that of the rate of strain:

$$Q = \frac{1}{2}\left(|\Omega_{ij}\Omega_{ij}|^2 - |S_{ij}S_{ij}|^2\right) > 0 \tag{16}$$

Using this criterion, vortices in any LES computation can be detected and visualized by rendering iso-surfaces of a given Q threshold.
Figure 18 represents, for the three operating conditions, iso-surfaces of the Q-criterion in the range between 10^4 and 10^6. These maps have been rendered from an instantaneous representation of the flow field in the stator region for every case. Despite the evident difficulty to analyze these coherent structures in such 2D images (vortices are covering each other and it is impossible to track a large number of vortices simultaneously), a closer look can reveal some relevant aspects of the vortical motion. Firstly, there is a noticeable difference between the rotor wakes depending on the flow rate. The evident widening of the wakes as the flow rate decreases is associated to larger vortices and more twisted filaments of vorticity. In particular, the vortical structures of rotor wakes are clearly visible for the nominal flow rate (top), even two or three stator chords downstream. Stretched, elliptical blobs of vorticity appear to be transported inactively through the stator passages. At off-design conditions (85% Q_N), vortex filaments begin to interact between consecutive lattices of wakes as well as with stator wakes, increasing the disorder of coherent structures. Vortices roll up close to the PS of the vanes (see the middle vane in the central figure), establishing an internal path due to the difference between the turn-out time of the incoming vortices and the time required by the flow to pass along the vanes. At near-stall conditions (70% Q_N), wakes exhibit a clear meandering behavior when impinging onto the vanes. Moreover, the coherent structures for rotor wakes are revealed as long filaments which completely cover the stator passage when convected through the vanes. Secondly, the reorientation of the vortical structures is another significant feature that is modified with the flow rate. Notice how the elliptical blobs of vorticity at nominal flow rate are aligned with the axial direction and how they hardly interact with small-scale vortices shed from the narrow stator wakes. As the flow rate is reduced, the reorientation of the filaments attains more complexity, with the detached flow conditions at 70% Q_N being the most evident example. In that case, the stator wakes are completely masked in a sea of highly stretched and chaotic collection of filaments with no preferable direction. Also, the coherent vortex shedding on the suction side of the vanes is identified in the representation of iso-Q surfaces for near-stall conditions. Especially for the upper and central vanes, three rolling-up vortices

- close to disruption - reveal the large detached flow region shielded from the impact of rotor wakes.

5.3.1. Integral length scales

This paper is concluded by presenting an estimation of the integral length scales (ILS) of the stator flow. The ILS of the largest eddies of the flow was determined by evaluating the correlation coefficient of the instantaneous velocity fluctuations (in time) for every computational cell. Again, we benefit from the large turbulent scales resolved in time by the LES closure to compute this variable. Theoretically, the area under the correlation gives the value of the ILS:

$$ILS = \bar{u} \int_0^\infty \rho(\tau) d\tau \tag{17}$$

being $\bar{u}$ the characteristic throughflow velocity and $\rho(\tau)$ the autocorrelation coefficient of the velocity fluctuations in time.

However, because this method is limited in practice, the criterion suggested by Tropea et al. [28] has been followed, accounting only for the energy until the first local minimum is reached.

Figure 19 compares the numerical results from LES computations with the experimental estimations from hot-wire measurements. At the bottom, the available maps in the experimental window and the CFD vane-to-vane plane data are shown for near-stall conditions, using identical scales to make the comparison easier. The experimental window presents low values outside the stator wakes, in the range of roughly 15-20 mm, which increase in the stator wakes to 25-30 mm due to the larger size of the vortices shed from the stator at 70% Q_N. Moreover, the region of detached flow is identified at 70% of the span (point D on the dashed white line) with maximum values in the order of 50 mm, where massive separations were previously found at shedding frequencies below the BPF. Note the similar mechanism with large values in the shear region close to the same location for point D in the case of the numerical plane. Finally, both numerical and experimental values of the ILS are compared at the tangential dashed line, corresponding to the 70% span of the radial coordinate, for the entire simulated database (Figure 19, top). Values at the stator wakes exhibit great similarities between both methodologies, with the lowest values around 5 mm for the vane wakes at nominal (100%) and partial-load (85%) cases. The wakes at 70% Q_N present higher values, up to 10-15 mm. In the regions between the wakes, the CFD is slightly overpredicting the size of the largest scales with respect to the experimental values.

6. Conclusions

In this work, LES computations of the rotor-stator Interaction in an axial fan stage for different operating conditions have been successfully modeled. Firstly, useful guidelines for statistical convergence of the time-resolved flow in case of

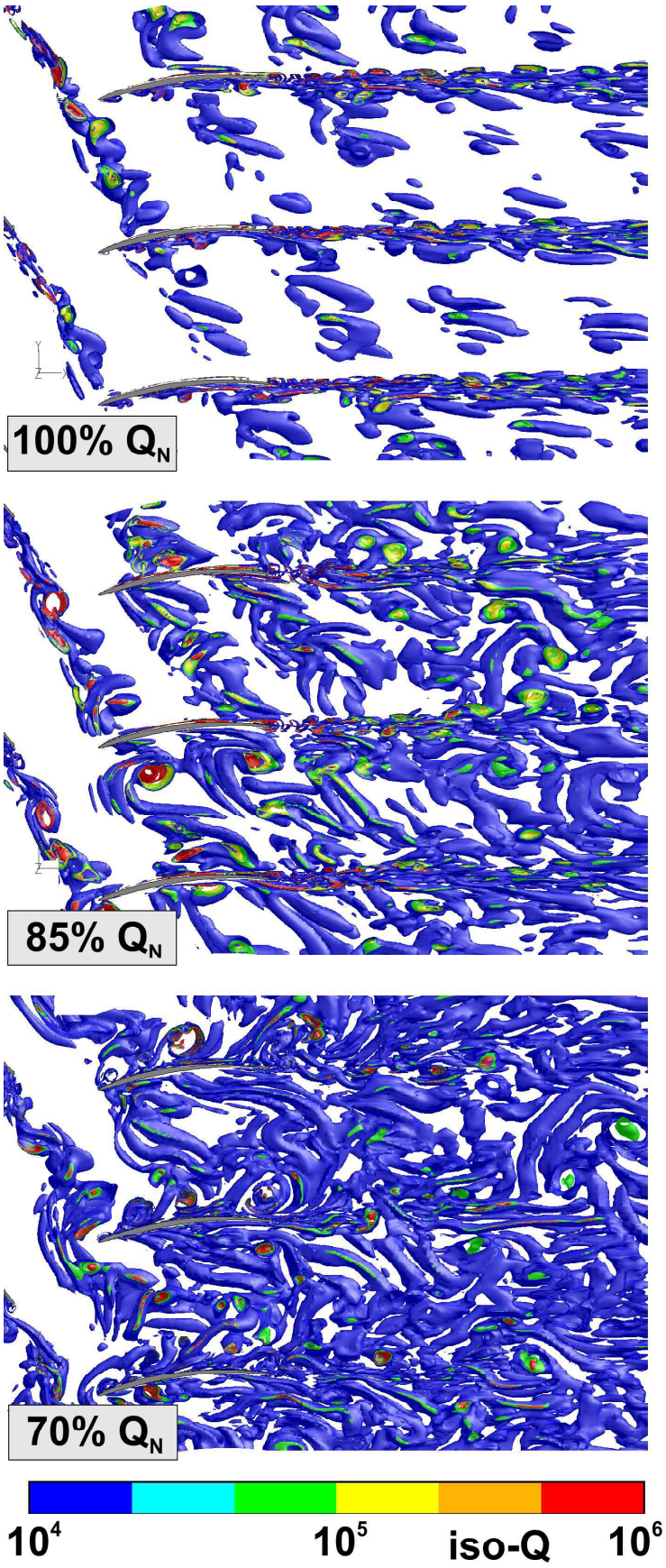

Figure 18: Identification of coherent structures (vortices) using the Q-criterion for different flow rates.

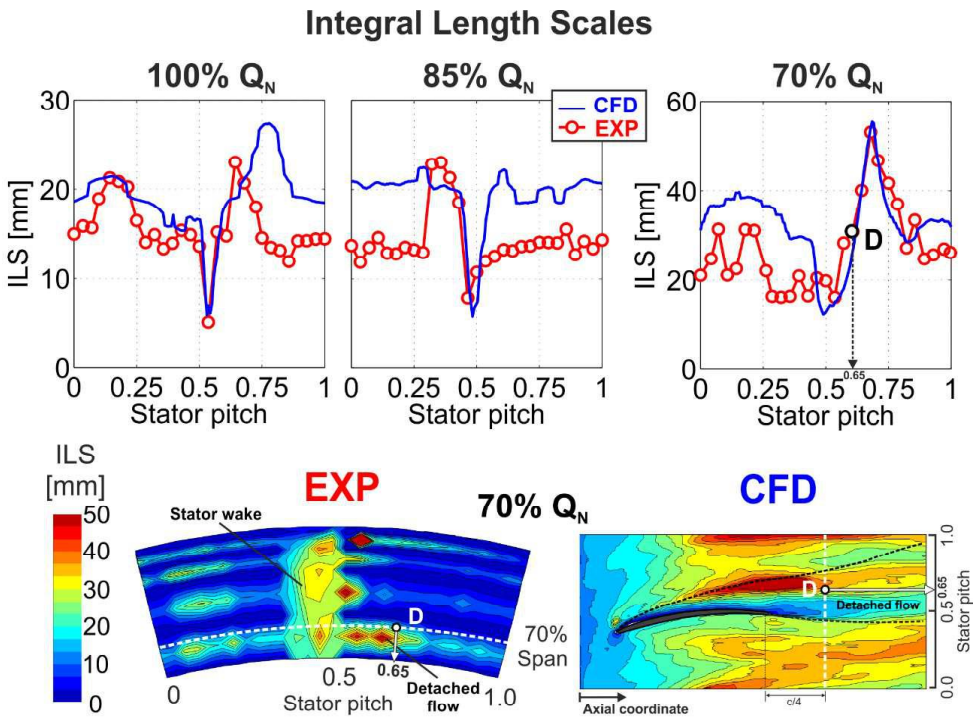

Figure 19: Distribution of Integral Length Scales for different flow rates. Experimental and numerical maps (bottom) and comparison of results at referring line at 70% (top).

multistage unsteady environments have been provided. The time-averaged turbulence level has shown to be the key parameter determining the number of ensemble averages required to ensure a given convergence threshold. Also, the entire database of numerical computations have been experimentally validated using hot-wire measurements from the real fan geometry at the stator exit. The essential mechanisms for rotor wake transport, interaction of stator boundary layers with turbulent wakes and induced vortex shedding as a function of flow rate have been perfectly captured with the numerical cascade model. Following, the analysis of the transport of rotor wakes and both wake-vane and wake-wake interactions in the stator flow field has been completed as the main objective of this paper. Special attention has been devoted to off-design conditions, where the description of massive flow separations from the SS of the vanes fully benefits from LES performance. It has been illustrated how the rotor wakes, impinging on the vanes, generate a coherent shedding of large-scale vortices at reduced frequencies (between 0.1 to 0.25 of the BPF). Meanwhile, the pressure coefficient in the vanes remains practically unaffected by this effect in the separated region. On the other hand, at nominal conditions, two spots of turbulence generation on the PS of the vanes are drastically conditioned by the rotor wakes, modifying the pressure coefficient on the leading edge of the vanes. The analysis of the flow patterns has given additional insight into the performance of the stator in the fan stage. Meantime flow structures have revealed that the stagger angle of the stator vanes is excessive for the nominal flow conditions of the rotor, while off-design operation of the fan demands a higher camber angle for the vanes. With respect to the instantaneous maps, the representation of the iso-Q crite-

rion highlighted the vortical nature of the flow and how the turbulent structures are convected and disrupted while mixing in the stator passages. Moreover, typical ILS sizes have been also provided, both within the wakes and in those calm regions with a low turbulence level, exhibiting reasonable agreement with experimental measurements. Turbulent scales and wake profiles, both meantime and time-resolved, have validated the adopted numerical framework. In addition, the detailed analysis of the off-design conditions demonstrates the accurate description of coherent vortical structures and length scales using LES computations. LES simulations have shown to be appropriate for the assessment of the design of an axial fan, especially for specific operating conditions for which a URANS model is unable to model turbulence with the required accuracy.

References

[1] A. Corsini, G. Delibra, and A.G. Sheard. A critical review of computational methods and their application in industrial fan design. *ISRN Mechanical Engineering*, 2013:625175, 2013.

[2] D. Borello, A. Corsini, G. Delibra, M. Fiorito, and A.G. Sheard. Large-eddy simulation of a tunnel ventilation fan. *Journal of Fluids Engineering*, 135:071102, 2013.

[3] J. Adamczyk. Aerodynamic analysis of multistage turbomachinery flow in support of aerodynamic design. *ASME Journal of Turbomachinery*, 122(2):189–217, 2000.

[4] U. Piomelli. *Large Eddy Simulation and Related Techniques. Lecture Series 2006-04.* Von Karman Institute for Fluid Dynamics, 2006.

[5] S.B. Pope. *Turbulent Flows.* Cambridge University Press, UK, 2000.

[6] U. Piomelli and E. Balaras. Wall-layer models for large eddy simulations. *Annual Review of Fluid Mechanics*, 34:349–374, 2002.

[7] N. Gourdain, F. Sicot, F. Duchaine, and L. Gicquels. Large eddy simulation of flows in industrial compressors: a path from 2015 to 2035. *Philosophical Transactions of the Royal Society A*, 372:20130323, 2014.

[8] P. Tucker, S. Eastwood, C. Klostermeier, R. Jefferson-Loveday, J. Tyacke, and Y.Liu. Hybrid LES approach for practical turbomachinery flows - Part I: Hierarchy and example simulations. *Journal of Turbomachinery*, 134(2):021023, 2012.

[9] P. Tucker. Computation of unsteady turbomachinery flows: Part 2 -LES and hybrids. *Progress in Aerospace Sciences*, 47(7):546–569, 2011.

[10] W.A. McMullan and G.J. Page. Towards large eddy simulation of gas turbine compressors. *Progress in Aerospace Sciences*, 52(12):30–47, 2012.

[11] D. Papadogiannis, F. Duchaine, L. Gicquel, G. Wang, and S. Moreau. Effects of subgrid scale modeling on the deterministic and stochastic turbulent energetic distribution in large-eddy simulations of a high-pressure turbine stage. *Journal of Turbomachinery*, 138(9):091005, 2016.

[12] G. Wang, F. Duchaine, D. Papadogiannis, I. Duran, S. Moreau, and L.Y.M. Gicquel. An overset grid method for large eddy simulation of turbomachinery stages. *Journal of Computational Physics*, 274:333–355, 2014.

[13] M. Zauner, N.D. Sandham, A.P.S. Wheeler, and R.D.Sandberg. Linear stability prediction of vortex structures on high pressure turbine blades. *International Journal of Turbomachinery Propulsion and Power*, 2(2):8, 2017.

[14] N. Odier, F. Duchaine, L.Y.M Giquel, G. Dufour, and N. García Rosa. Comparison of LES and RANS predictions with experimental results of the fan of a turbofan. In *Proceedings of the 12th European Turbomachinery Conference*, pages ETC2017–126, Stockholm, Sweeden, Apr 2017.

[15] L. Davidson and S. Dahlström. Hybrid LES-RANS: An approach to make LES applicable at high Reynolds numbers. *International Journal of Computational Fluid Dynamics*, 19(6):415–427, 2005.

[16] K.M. Argüelles Díaz, J.M Fernández Oro, M. Galdo Vega, and E. Blanco Marigorta. Effects of prong-wire interferences in dual hot-wire probes on the measurements of unsteady flows and turbulence in low-speed axial fans. *Measurement*, 91:1–11, 2016.

[17] M. Galdo Vega, J.M. Fernández Oro, K.M. Argüelles Díaz, and C. Santolaria Morros. Effect of rotor-stator configuration in the generation of vortical scales and wake mixing in single stage axial fans: Part I - LES modelling and experimental validations. In *Proceedings of the ASME 2013 Fluids Engineering Division Summer Meeting*, page V01AT02A005; 13 pages, Incline Village, Nevada, USA, Jul 2013. ASME.

[18] S.Lee, H.-J. Kim, and A. Runchal. Large eddy simulation of unsteady flows in turbomachinery. *Proceedings of the Institution of Mechanical Engineers, Part A: Journal of Power and Energy*, 218:463–475, 2004.

[19] A. Arnone, M. Marconcini, A. Scotti Del Greco, and E. Spano. Numerical investigation of three-dimensional clocking effects in a low pressure turbine. *ASME Journal of Turbomachinery*, 126(3):375–384, 2004.

[20] J.M. Fernández Oro, K.M. Argüelles Díaz, C. Santolaria Morros, and E. Blanco Marigorta. On the structure of turbulence in a low-speed axial fan with inlet guide vanes. *Experimental Thermal and Fluid Science*, 32(8):316–331, 2007.

[21] Y. Chen, X. Chen, J. Li, Z. Gong, and C. Lu. Large eddy simulation and investigation on the flow structure of the cascading cavitation shedding regime around 3d twisted hydrofoil. *Ocean Engineering*, 129:1–19, 2017.

[22] D.R. Chapman. Computational aerodynamics development and outlook. *AIAA Journal*, 17(12):1293–1313, 1979.

[23] S. Lieblein. Incidence and deviation-angle correlations for compressor cascades. *Journal of Basic Engineering*, 82(3):575–584, 1960.

[24] J.M. Fernández Oro, K.M. Argüelles Díaz, and E. Blanco Marigorta. Non-deterministic kinetic energy within the rotor wakes and boundary layers of low-speed axial fans: Frequency-based decomposition of unforced unsteadiness and turbulence. *Journal of Turbulence*, 10:N28, 2009.

[25] O. Uzol, D. Brzozowski, Y.-C. Chow, J. Katz, and C. Meneveau. A database of PIV measurements within a turbomachinery stage and sample comparisons with unsteady RANS. *Journal of Turbulence*, 8:N10, 2007.

[26] J.M. Fernández Oro, K.M. Argüelles Díaz, M. Rodríguez Lastra, M. Galdo Vega, and B. Pereiras García. Converged statistics for time-resolved measurements in low-speed axial fans using high-frequency response probes. *Experimental Thermal and Fluid Science*, 54:71–84, 2014.

[27] G. Haller. An objective definition of a vortex. *Journal of Fluid Mechanics*, 525:1–26, 2005.

[28] C. Tropea, A. Yarin, and J. Foss. *Handbook of Experimental Fluid Mechanics*. Springer-Verlag Berlin Heidelberg, 2007.